The 2021 M_w 7.4 Madoi earthquake: an archetype bilateral slip-pulse rupture arrested at a splay fault

Kejie Chen[1], Jean-Philippe Avouac[2], Jianghui Geng[3], Cunren Liang[4], Zhenguo Zhang[1], Zhicai Li[5],

Shengpeng Zhang[6,7]

1 Department of Earth and Space Sciences, Southern University of Science and Technology, Shenzhen, 518055, Guangdong, China

2 Division of Geological and Planetary Sciences, California Institute of Technology, Pasadena, CA, 91125, USA

3 GNSS Resarch Center, Wuhan University, Wuhan, 430079, Hubei, China

4 School of Earth and Space Sciences, Peking University, Beijing, 100871, China

5 School of Geoscience and Surveying Engineering, China University of Mining and Technology-Beijing, Beijing 100083, China

6 School of Geographic Science, Qinghai Normal University, Xining 810008, China

7 Qinghai Basic Surveying and Mapping Institute, Xining 810101, China

Abstract

We combine measurements of ground deformation from Synthetic Aperture Radar images, high-rate GNSS and tele-seismic waveforms to study the rupture kinematics of the Madoi earthquake, which occurred in eastern Tibet on May 21, 2021 and reached a moment magnitude M_w 7.4. The data show nearly pure left-lateral motion along a 170 km long rupture and a total duration of 36s. The earthquake initiated near the middle of the main segment and evolved in a bilateral slip pulse rupture which propagated at a sub-Rayleigh speed of 2.6-2.8 km/s. In our model, slip is concentrated at depth of less than ~15 km and reaches a maximum of 4.2 m. The rupture arrested ~10 s after branching on the extensional splay faults at both extremities. The branching onto the splay faults and the eventual arrest of the rupture is used to provide constraints on the fault frictional properties.

Key points:

- The 2021 M_w 7.4 Madoi earthquake ruptured bilaterally for about 170 km with most of slip being concentrated at less than 15 km depth

- The rupture was arrested after propagating on splay faults

- Propagation along the most misoriented splay fault suggests a dynamic friction possibly as low as 0.05

Plain language summary:

The M7.4 Madoi earthquake, which occurred in eastern Tibet on May 21, 2021 is the largest event since the 2008, M8.0 Wenchuan earthquake. It therefore generated widespread interests among the Chinese public and scientific community. Here, we model the temporal evolution of fault slip during the earthquake using geodetic and seismic observations. Our study reveals a slip-pulse that ruptured a 170 km long fault system, extending from the surface to about 15 km at depth, with horizontal shear slip of up to 4.2 m. The rupture initiated near the middle of the ruptured fault, propagated bi-laterally along the fault trace, and ended after branching on splay-faults. Forking seems to have arrested the rupture. The Madoi earthquake relates to the eastward extrusion of Tibet which is driven by the northward indentation of India into Eurasia.

1. Introduction

On May 21, 2021, a widely felt earthquake struck the Madoi County in Qinghai province, eastern Tibet, China. Its surface wave magnitude was estimated to M_s 7.4 (https://www.cea.gov.cn/cea/dzpd/index.html). The epicenter determined by the China Earthquake Administration, 98.34°E, 34.59°N, is located in a pastoral and sparsely populated area (Figure 1a). No casualty or severe damage was reported. A network of Global Navigation Satellite System (GNSS) stations (Figure 1b) operated continuously, recorded the ground motion at a rate of >=1 sample per second [*Li et al.*, 2021]. Such high

rate (HR)-GNSS stations provide displacement waveforms covering a broad spectrum from DC (the static displacement) to the Nyquist frequency determined by the sampling rate [*Bock et al., 2011*]. The noise levels are high (usually at ~1-2 cm), but such records don't suffer from the baseline offsets that limit inertial instruments [*Ruhl et al., 2017*]. HR-GNSS records can therefore provide unique insight into the rupture process [e.g., *Galetzka et al.*, 2015; *Kaneko et al.*, 2017; *Weng and Yang*, 2018; *Liu et al.*, 2019; *Chen et al.*, 2020]. To date, only a handful of earthquakes have occurred at distances close enough to HR-GNSS stations to yield displacement waveforms well above the noise level [*Ruhl et al.*, 2019].

The ground motion signal of the Madoi earthquake recorded by 14 HR-GNSS stations located within about 200 km from the epicenter (Figure 1b) is well above the noise level. These displacement waveforms thus provide an exceptional opportunity to characterize the rupture kinematics, particularly when complemented by the tele-seismic records and remote sensing observations of near-field ground deformation, which are more commonly used to determine earthquake source model [e.g., *Li et al.*, 2011].

In this study, we determine the rupture kinematics of the 2021 M7.4 Madoi earthquake from the joint inversion of synthetic aperture radar (SAR) interferograms, static GNSS offsets, high-rate (1 Hz) GNSS and broadband tele-seismic P waveforms. We first present the data and methods used in this study, then describe the results obtained from a kinematic joint inversion of these data. Finally, we comment on some key features of our source

model, draw some implications for earthquake dynamics, and discuss the tectonic significance of this earthquake.

2. Data and Methods

We use both interferometric SAR (InSAR) [*Rosen et al.*, 2000] and amplitude cross-correlation [*Michel et al.*, 1999] to measure the static deformation caused by the earthquake. InSAR makes use of the phase of the SAR data to provide a measurement of the displacement along the line of sight of the satellite. It is more accurate than cross-correlation, but it commonly suffers from decorrelation, especially where large deformation or severe ground shaking occurred. The fault geometry is therefore determined using the amplitude cross-correlation results at the surface (see Figure 1b and supplemented Figure S1a). The catalog of relocated aftershocks of *Wang et al.* [2021] (Figure 1c) and moment tensor solutions (Table 1) are used to help constrain the fault at depth.

We use Sentinel-1 SAR data acquired on both ascending (track 99 from May 20, 2021 to May 26, 2021) and descending tracks (track 106 from May 20, 2021 to May 26, 2021). The data were processed with the ISCE software [*Rosen et al.*, 2012] and downsampled using a quadtree algorithm [*Jónsson et al.*, 2002] (see Figure S1). Specifically, we use statistical-cost network-flow algorithm for phase unwrapping to unwrap the interferograms. Before unwrapping, the ruptured areas are masked out and smooth-solution mode costs and minimum-cost flow algorithm is adopted for initialization. To gain insight into the time evolution of fault slip we also use 1 Hz displacement waveforms recorded at 14 GNSS

stations (Figure 1b and Figure S5) [*Gérard and Luzum*, 2010; *Rebischung and Schmid*, 2016; *Geng et al.*, 2019] and P-wave records at 20 broadband seismic stations (Figure S5)[*Dziewonski and Anderson*, 1981]. Detailed information about the data processing and preparation is provided in the supplementary material (Text S1).

To determine the rupture kinematics, we invert the joint dataset using a linear inversion scheme. The Green's functions for GNSS displacements and InSAR offsets are calculated with the frequency-wavenumber integration method [*Zhu and Rivera, 2002*] using a 1-D layered velocity model (see Table S3) derived from CRUST 2.0 (https://igppweb.ucsd.edu/~gabi/crust2.html) [*Bassin et al.*, 2000]. The teleseismic Green's functions are produced through a propagator matrix approach [*Kikuchi and Kanamori*, 1982]. A non-negative least squares inversion is employed which allows for variations of rake and slip amplitude (the allowed range of values are listed in Table S2). We use five symmetric triangles with 2 s half-durations staggered by 1 s for each sub-fault to allow for a possibly complex source time function. We employ a Laplacian regularization to ensure spatiotemporal stability of the inversion result, and impose no slip at the bottom edge of the fault. We test different rupture speeds from 1.6 km/s to 3.6 km with 0.2 km/s intervals.

We adjust the weight assigned to each kind of data using an iterative procedure [e.g., *Konca et al.*, 2010; *Chen et al.*, 2018]: prior uncertainties are rescaled so that each dataset is fit equally well, i.e., with residuals amounting to a similar proportion of the uncertainties. As a result, we find weighting stable factors of 1:1:1:2 assigned to the static GNSS offsets, high-rate GNSS, P waveforms and InSAR.

3. Results

The amplitude correlation results show a sharp, WNW-trending discontinuity with a relatively straight central segment and secondary segments splaying off the main fault at both rupture termination locations. This makes a nearly symetrical fault trace centered approximately on the epicenter (see Figure 1b). Based on the fault trace mapped from the SAR offests we subdivided the fault into 4 planar segments (labeled F1, F2, F3 and F4 in Figure 2a) with varying strike. F2 is the main segment and the observations suggest mostly strike-slip motion. The SAR offset data suggest that the main fault F2 splays into two faults, F3 and F4, at its ESE termination, and into F1 at its WNW termination. In both cases, these splay-faults lie on the extensional side of the main fault given the purely left-lateral motion on F2.

The aftershocks [*Wang et al.,* 2021] span a depth range from 0 to 20 km. They do not align perfectly below the fault trace (Figure 1c and Figure S1a). *Wang et al.* [2021] suggest a sub-vertical fault, but the moment tensor solutions from different seismological services are quite variable (Table S1). We thus vary the dip angles to determine the best-fit angle by trial and error. We test north and south dipping values from 70° to 90° at an interval of 2° for each fault segment. An 80° dip angle to the north fits the InSAR data best (see Figure S2). However, for segment F4, a north-dipping plane would fail to match the aftershocks distribution, and we therefore adopt a south-dipping angle for this fault segment. The final best-fitting fault geometries are described in Table S2.

The sensitivity test (Figure S3) shows that the overall best fitting rupture velocity is 2.6–2.8 km/s. The best-fitting slip model obtained from the joint inversion of all the data and the corresponding moment rate function are shown in Figure 3. The jackknife resolution test (Figure S4) suggests an uncertainty of about 20 cm at the 95% confidence level. The uncertainty gets higher below 20 km due to lower resoultion at depth. The model yields an excellent fit to the near field geodetic data (Figures 2, 3 and Figure S5), and variance reductions for static GNSS offsets, high-rate GNSS and InSAR measurements are 88.5%, 76.3%, 82.4% respectively. However, the fit to the vertical components of high-rate GNSS and P wave (variance reduction 45.2%) is relatively poor, probably due to the low signal-noise ratio arising from the strike-slip focal mechanism.

The best fitting model (see Figure 3) has a total seismic moment of 1.65×10^{20} Nm, equivalent to a moment magnitude of M_w 7.4, a duration of ~36 s seconds with a peak moment rate at ~25 s. The rupture is bilateral with the hypocenter located near the centroid of the slip distribution (Figure 3a). Overall, the source is distributed over a rather broad rupture area spanning an along-strike distance of 170 km and an along-dip distance from the surface to 20 km depth. Four asperities might be distinguished. Two asperities located to the southeast of the epicenter along F2 with >3 m and >4 m peak slips are located about ~30 km and ~80 km southeast of the hypocenter (Figure 3). The other two asperities with >2 m of slip are located ~ 30 km and ~70 km northwest of the hypocenter. Over 80% of the moment was released at depth less than 15 km depth, and substantial slip occurred near the surface, in agreement with the extensive surface ruptures observed in the field by the Qinghai Earthquake Agency (https://www.qhdzj.gov.cn/Item/2/19663.aspx). The rake

angles show nearly pure strike-slip motion on the main segment F2, and a small normal component on the splay faults F1 (see Figure 3a). The best double couple moment tensor fitting the sum of the moment tensor of all the elementary sources is consistent with the - 9° rake of global centroid- moment-tensor (GCMT) solution (Figure 2).

Snapshots of the rupture evolution are shown in Figure 4a, and an animation with a 1 s frame interval is provided in the supplementary movie M1. Until 7 s after the origin time, the rupture expanded updip and downdip around the hypocenter as a quasi-circular crack rupture. After that, it evolved into a bilateral pulse rupture with two clear slip pulses propagating toward the southeast and northwest at about 2.8 km/s. The largest slip rate in our model reached 1.5 m/s at 24 s, resulting a peak moment rate of 1.23×10^{19} Nm/s. It is probable that the slip rate was even faster given the high-pass filter applied to the waveforms and the spatial smoothing resulting from the Laplacian regularization of the inversion. The slip pulses attenuated rapidly as they reach the extensional splay faults F1, F3 and F4, leading to an abrupt drop of the moment rate function over the period from ~25 s to ~36 s.

4. Discussion and Conclusion

The data assembled in this study reveal a remarkably simple rupture kinematics at the first order. It shows a nearly symmetrical bilateral slip-pulse rupture of a rather straight near-vertical main fault segment with purely strike-slip motion. The width of the slip pulse is about 5 km corresponding to a rise time of less than 5 s. Because frequencies higher than 0.4 Hz were filtered out due to the noise level of the HR-GNSS records, and because of the

spatial smoothing resulting from the Laplacian regularization, it is possible that the rise time is even shorter and the pulse narrower. The average rupture velocity of 2.8 km/s is 80% the Rayleigh wave speed estimated using the velocity structure at depth less than 18 km derived from CRUST 2.0 (Table S3). Noteworthily, the rupture branched onto extensional splay faults both toward the WNW (F1) and toward the ESE (F3, F4) and arrested rapidly afterwards.

This overall behavior is consistent with theoretical model of the source of strike-slip earthquake as mode II rupture, accelerating toward the Rayleigh wave speed, and the tendency to branch to extensional splay faults and arrest [e.g., *Poliakov et al.*, 2002]. Slip-pulses can form in numerical simulations if the fault friction weakens significantly during slip [*Beeler and Tullis*, 1996; *Lu et al.*, 2007] or due to a geometric control, in presence of stress heterogeneities or if the fault is elongated along the direction of propagation of the rupture [e.g., *Day*, 1982; *Beroza and Mikumo*, 1996]. Both explanations could in principle apply to the Madoi earthquake. Another interesting observation is that the rather straight geometry of the main fault segment (F2) could have favored a super-shear rupture. i.e. a rupture propagating faster than the S waves [*Bouchon et al.*, 2010]. To assess the possibility of a super-shear component, it is instructive to look at the fault normal (FN) and fault parallel (FP) displacement waveforms. According to theory and experiments [*Dunham et al.*, 2005; *Mello et al.*, 2016], a sub-Rayleigh rupture should show dominantly FN pulse, while a supershear rupture should show a dominantly FP motion. We therefore check the FN and FP displacement waveforms, calculated based on the 285.9° strike of the main fault segment F2, at the two stations closest to the rupture, QHMD and QHAJ,

which lay respectively at 29 km and 15 km from the fault trace (Figure 3b). The record at QHAJ shows a larger FN velocity and an overall SSW direction of motion (Figure 4b). These two characteristics are typically indicative of sub-Rayleigh rupture. The record at QHMD is more ambiguous though. This analysis might be refined using accelerometric records.

The arresting effect of branching on splay faults is also a feature expected from theory and numerical simulations [e.g., *Kame and Yamashita*, 1999; *Aochi et al.*, 2003; *Kase and Day*, 2006]. The observation that the rupture was able to branch to a splay fault but rapidly arrested suggests that the initial shear stress on this splay fault was close to the residual shear strength, *i.e.,* the strength after the drop from static to dynamic friction. Following the reasoning presented by [*Aochi et al.*, 2003] for a quasistatic rupture process, it is then possible to derive constraints on fault friction. To do so, we assume a homogeneous stress field and a main fault optimally oriented for failure. With this logic (illustrated in Figure S6) we get the following equation,

$$\mu_d = tan\varphi_d = \frac{\cos(\varphi_d+2\theta)}{\frac{1}{sin\varphi_s}-\sin(\varphi_s+2\theta)} \tag{1}$$

where $\mu_s = tan\varphi_s$ is the static friction, $\mu_d = tan\varphi_d$ is the dynamic friction and θ is the angle between the main fault segment and the splay fault, positive toward the extensional domain. The splay faults F1, F3 and F4 strike respectively 11.5°, 28° and 6° away from the main fault F2. Assuming a static friction of 0.6, the bend of 28 degree (F3) would mean a dynamic friction as low as 0.05. The other splay faults (11.5° for F1 and 6° for F4) imply higher values of ~0.54 and 0.46. These estimates are to be considered with caution and are presented here to illustrate how, in principle, our observations can be used to help constrain

fault friction. Note that a dynamic friction as low as 0.05, if it were representative of friction on the whole fault system could explain the formation for a self-healing pulse but would imply a static stress drop probably unrealistically large.

The fault activated during the Madoi earthquake was actually already known as the Jiangcuo fault [*Zhu et al.*, 2021]. Left-lateral motion on this fault is consistent with the regional tectonics of eastern Tibet which is dominated by left-lateral strike-slip motion on major faults with similar EW to NE-SW strike including the Kunlun fault, the Haiyuan and the Xianshuihe faults [*Tapponnier et al.*, 2001] (Figure 1). These faults delimit blocks that are extruded eastwards out of the way of indenting India and rotate clockwise (Figure 1a) [*England and Molnar*, 1990; *Avouac and Tapponnier*, 1993]. The fault activated during the Madoi earthquake is parallel and close to the Kunlun fault which marks the northern edge of the Bayan Har Block (see Figure 1a). The slip rate of this fault is estimated to no more than 6-8 mm from tectonic geomorphy [*Xiong et al.*, 2010] and interseismic strain is undetectable from 2015-2020 InSAR timeseries as shown by *Zhao et al.* [2021]. The Madoi earthquake appears as the latest event in a sequence of M>7 events which have ruptured at the boundaries of this block. The sequence started with the 1997 M7.5 Mani earthquake and included the 2001 M8.1 Kunlun and 2008 M8.0 Wenchuan earthquakes (Figure 1a). The 1997 M7.5 Mani and 2010 M7.1 Yushu events occurred on the southern boundary of the Bayan Har active block. The 2008 M8.0 Wenchuan earthquake, 2013 M7.0 Lushan earthquake and the 2017 Jiuzhaigou M7.0 earthquake occurred at the eastern boundary of the Bayan Har block. The 2001 M8.1 Kunlun earthquake occurred along its northern boundary. The 2008 M7.4 and 2014 M7.3 Yutian earthquakes were located at its

western end. Remarkably, all the M>=7 events in China since 1997 occurred on the faults bounding the Bayan Har block. The Madoi earthquake however occurred on a second fault located south of the Kunlun fault and is a manifestation of internal deformation within the Bayan Har block.

5. Conclusion

Thanks to the availability of quality remote sensing and high rate GNSS data we were able to constrain the fault geometry and kinematics of rupture during the Madoi earthquake. The earthquake appears as a simple bi-lateral sub-Rayleigh rupture that conforms the standard theory of earthquake dynamics. We used a simple quasi-static representation of the rupture to illustrate how our observations relate to the fault frictional properties but our inferences would need to be refined based on dynamic modeling. The earthquake appears to part of a cluster of large (M_w>=7.0) events associated to the Bayan Har block.

Open Research

Original Copernicus Sentinel-1 data were acquired by the European Space Agency (https://scihub.copernicus.eu/) and downloaded from the Alaska Satellite Facility (https://search.asf.alaska.edu/#/). GNSS stations QHMD and QHMQ were operated by the Crustal Movement Observation Network of China (CMONOC), and other GNSS data were from the continously operating reference stations network operated by the local government [*Li et al.*, 2021]. Teleseimic waveforms were obtained through the Data Management Center of the Incorporated Research Institutions for Seismology (https://ds.iris.edu/wilber3/find_stations/11417068). All of the links are last accessed 2021 June and the SAR data are stored at https://doi.org/10.5281/zenodo.5090461, and high-rate GNSS in Seismic Analysis Code (SAC) format is provided in the supplementary dataset. The prefered slip model parameters are listed in supplementary Table S4. Most of the figures in this paper were prepared using Generic Mapping Tools [Wessel et al., 2013].

References

Aochi, H., R. Madariaga, and E. Fukuyama (2003), Constraint of fault parameters inferred from nonplanar fault modeling, *Geochemistry, Geophys. Geosystems*, *4*(2), 1–16, doi:10.1029/2001GC000207.

Avouac, J. -P, and P. Tapponnier (1993), Kinematic model of active deformation in central Asia, *Geophys. Res. Lett.*, doi:10.1029/93GL00128.

Bassin, C., G. Laske, and G. Masters (2000), The current limits of resolution for surface wave tomography in North America, *EOS Trans AGU*, *81*, 897, doi:Eos Trans. AGU.

Beeler, N. M., and T. E. Tullis (1996), Self-healing slip pulses in dynamic rupture models due to velocity-dependent strength, *Bull. Seismol. Soc. Am.*, *86*(4), 1130–1148, doi:10.1785/BSSA0860041130.

Beroza, G. C., and T. Mikumo (1996), Short slip duration in dynamic rupture in the presence of heterogeneous fault properties, *J. Geophys. Res. Solid Earth*, *101*(B10), 22449–22460, doi:10.1029/96jb02291.

Bock, Y., D. Melgar, and B. W. Crowell (2011), Real-Time strong-motion broadband displacements from collocated GPS and accelerometers, *Bull. Seismol. Soc. Am.*, *101*(6), 2904–2925, doi:10.1785/0120110007.

Bouchon, M., H. Karabulut, M.-P. Bouin, J. Schmittbuhl, M. Vallée, R. Archuleta, S. Das, F. Renard, and D. Marsan (2010), Faulting characteristics of supershear earthquakes, *Tectonophysics*, *493*(3–4), 244–253, doi:10.1016/j.tecto.2010.06.011.

Chen, K., Z. Liu, C. Liang, and Y. T. Song (2018), Towards the application of seismogeodesy in central Italy: a case study for the 2016 August 24 Mw 6.1 Italy earthquake modelling, *Geophys. J. Int.*, *213*(3), 1647–1658, doi:10.1093/gji/ggy089.

Chen, K., J. Avouac, S. Aati, C. Milliner, F. Zheng, and C. Shi (2020), Cascading and pulse-like ruptures during the 2019 Ridgecrest earthquakes in the Eastern California Shear Zone, *Nat. Commun.*, *11*(1), 22, doi:10.1038/s41467-019-13750-w.

Day, S. M. (1982), Three-dimensional simulation of spontaneous rupture: The effect of nonuniform prestress, *Bull. Seismol. Soc. Am.*, *72*(6A), 1881–1902, doi:doi.org/10.1785/BSSA07206A1881.

Deng, Q., P. Zhang, Y. Ran, X. Yang, W. Min, and L. Chen (2003), Active tectonics and earthquake activities in China, *Earth Sci. Front.*, *10*(S1), 66–73.

Dunham, E. M. (2005), Near-source ground motion from steady state dynamic rupture pulses, *Geophys. Res. Lett.*, *32*(3), L03302, doi:10.1029/2004GL021793.

Dziewonski, A. M., and D. L. Anderson (1981), Preliminary reference Earth model, *Phys. Earth Planet. Inter.*, *25*(4), 297–356, doi:10.1016/0031-9201(81)90046-7.

England, P., and P. Molnar (1990), Right-lateral shear and rotation as the explanation for strike-slip faulting in eastern Tibet, *Nature*, *344*(6262), 140–142, doi:10.1038/344140a0.

Galetzka, J. et al. (2015), Slip pulse and resonance of the Kathmandu basin during the 2015 Gorkha earthquake, Nepal, *Science (80-.).*, *349*(6252), 1091–1095, doi:10.1126/science.aac6383.

Geng, J., X. Chen, Y. Pan, S. Mao, C. Li, J. Zhou, and K. Zhang (2019), PRIDE PPP-AR: an open-source software for GPS PPP ambiguity resolution, *GPS Solut.*, doi:10.1007/s10291-019-0888-1.

Gérard, P., and B. Luzum (2010), IERS Conventions (2010), *Bur. Int. Des Poids Mes. Sevres*.

Jónsson, S., H. Zebker, P. Segall, and F. Amelung (2002), Fault slip distribution of the 1999 Mw 7.1 Hector Mine, California, earthquake, estimated from satellite radar and GPS measurements, *Bull. Seismol. Soc. Am.*, *92*(4), 1377–1389, doi:10.1785/0120000922.

Kame, N., and T. Yamashita (1999), A new light on arresting mechanism of dynamic earthquake faulting, *Geophys. Res. Lett.*, *26*(13), 1997–2000.

Kaneko, Y., E. Fukuyama, and I. J. Hamling (2017), Slip-weakening distance and energy budget inferred from near-fault ground deformation during the 2016 M w 7.8 Kaikōura earthquake, *Geophys. Res. Lett.*, *44*(10), 4765–4773, doi:10.1002/2017GL073681.

Kase, Y., and S. M. Day (2006), Spontaneous rupture processes on a bending fault, *Geophys. Res. Lett.*, *33*(10), 2–5, doi:10.1029/2006GL025870.

Kikuchi, M., and H. Kanamori (1982), Inversion of complex body waves, *Bull. Seismol. Soc. Am.*, *72*(2), 491–506.

Konca, A. O., S. Leprince, J.-P. Avouac, and D. V. Helmberger (2010), Rupture Process of the 1999 Mw 7.1 Duzce Earthquake from Joint Analysis of SPOT, GPS, InSAR, Strong-Motion, and Teleseismic Data: A Supershear Rupture with Variable Rupture Velocity, *Bull. Seismol. Soc. Am.*, *100*(1), 267–288, doi:10.1785/0120090072.

Li, Z., J. R. Elliott, W. Feng, J. A. Jackson, B. E. Parsons, and R. J. Walters (2011), The 2010 Mw 6.8 Yushu (Qinghai, China) earthquake: Constraints provided by InSAR and body wave seismology, *J. Geophys. Res.*, *116*(B10), B10302, doi:10.1029/2011JB008358.

Li, Z., K. Ding, P. Zhang, Y. Wen, L. Zhao, and J. Chen (2021), Co-seismic deformation and slip distribution Of 2021 Mw 7.4 Madoi earthquake from GNSS observation, *Geomatics Inf. Sci. Wuhan Univ.*, doi:10.13203/j.whugis20210301.

Liu, C., T. Lay, E. E. Brodsky, K. Dascher-Cousineau, and X. Xiong (2019), Coseismic Rupture Process of the Large 2019 Ridgecrest Earthquakes From Joint Inversion of Geodetic and Seismological Observations, *Geophys. Res. Lett.*, doi:10.1029/2019GL084949.

Lu, X., N. Lapusta, and A. J. Rosakis (2007), Pulse-like and crack-like ruptures in experiments mimicking crustal earthquakes, *Proc. Natl. Acad. Sci. U. S. A.*, doi:10.1073/pnas.0704268104.

Mello, M., H. S. Bhat, and A. J. Rosakis (2016), Spatiotemporal properties of Sub-Rayleigh and supershear rupture velocity fields: Theory and experiments, *J. Mech. Phys. Solids*, *93*, 153–181, doi:10.1016/j.jmps.2016.02.031.

Michel, R., J.-P. Avouac, and J. Taboury (1999), Measuring ground displacements from SAR amplitude images: Application to the Landers Earthquake, *Geophys. Res. Lett.*, *26*(7), 875–878, doi:10.1029/1999GL900138.

Poliakov, A. N. B., R. Dmowska, and J. R. Rice (2002), Dynamic shear rupture interactions with fault bends and off-axis secondary faulting, *J. Geophys. Res. Solid Earth*, *107*(B11), ESE 6-1-ESE 6-18, doi:10.1029/2001JB000572.

Rebischung, P., and R. Schmid (2016), IGS14/igs14.atx: a new Framework for the IGS Products, in *AGU Fall Meeting Abstracts*, vol. 2016, pp. G41A-0998.

Ruhl, C. J., D. Melgar, R. Grapenthin, and R. M. Allen (2017), The value of real-time GNSS to earthquake early warning, *Geophys. Res. Lett.*, *44*(16), 8311–8319, doi:10.1002/2017GL074502.

Ruhl, C. J. et al. (2019), A Global Database of Strong-Motion Displacement GNSS Recordings and an Example Application to PGD Scaling, *Seismol. Res. Lett.*, *90*(1), 271–279, doi:10.1785/0220180177.

Tapponnier, P., X. Zhiqin, F. Roger, B. Meyer, N. Arnaud, G. Wittlinger, and Y. Jingsui (2001), Oblique stepwise rise and growth of the tibet plateau, *Science (80-.).*, *294*(5547), 1671–1677, doi:10.1126/science.105978.

Wang, T., and S. Jónsson (2015), Improved SAR amplitude image offset measurements for deriving three-dimensional coseismic displacements, *IEEE J. Sel. Top. Appl. Earth Obs. Remote Sens.*, *8*(7), 3271–3278, doi:10.1109/JSTARS.2014.2387865.

Wang, W., L. Fang, J. Wu, H. Tu, L. Chen, G. Lai, and L. Zhang (2021), Aftershock sequence relocation of the 2021 MS7.4 Maduo Earthquake, Qinghai, China, *Sci. Sin. Terrae*, doi:10.1360/SSTe-2021-0149.

Weng, H., and H. Yang (2018), Constraining Frictional Properties on Fault by Dynamic Rupture Simulations and Near-Field Observations, *J. Geophys. Res. Solid Earth*,

123(8), 6658–6670, doi:10.1029/2017JB015414.

Wessel, P., W. H. F. Smith, R. Scharroo, J. Luis, and F. Wobbe (2013), Generic mapping tools: Improved version released, *Eos (Washington. DC).*, *94*(45), 409–410, doi:10.1002/2013EO450001.

Zhao, D., C. Qu, H. Chen, X. Shan, X. Song, and W. Gong (2021), Tectonic and Geometric Control on Fault Kinematics of the 2021 Mw7.3 Maduo (China) Earthquake Inferred From Interseismic, Coseismic, and Postseismic InSAR Observations, *Geophys. Res. Lett.*, *48*(18), 1–12, doi:10.1029/2021GL095417.

Zhu, L., and L. A. Rivera (2002), A note on the dynamic and static displacements from a point source in multilayered media, *Geophys. J. Int.*, *148*(3), 619–627, doi:10.1046/j.1365-246X.2002.01610.x.

Zhu, Y., F. Diao, Y. Fu, C. Liu, and X. Xiong (2021), Slip rate of the seismogenic fault of the 2021 Maduo earthquake in western China inferred from GPS observations, *Sci. China Earth Sci.*, *64*(8), 1363–1370, doi:10.1007/s11430-021-9808-0.
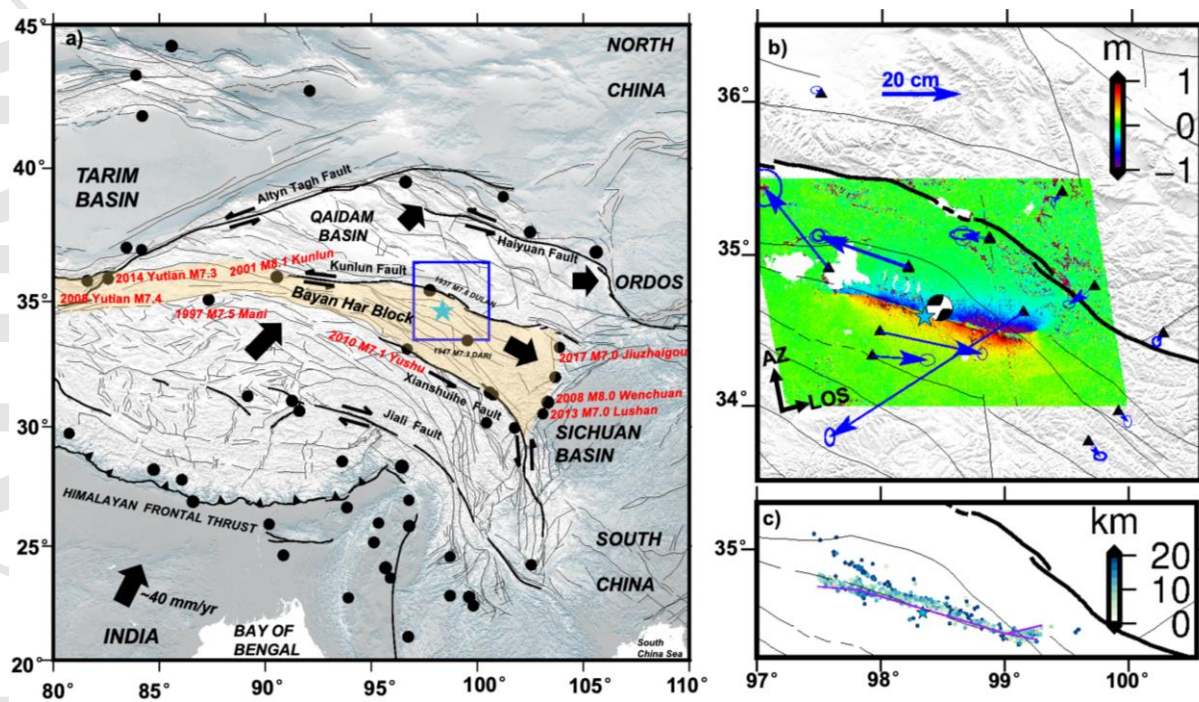
Figure 1. **a)** Tectonic setting of study area with M>=7 historical earthquakes (black dots, USGS) since 1900. The blue star is the epicenter of the 2021 M7.4 Madoi earthquake provided by the China Earthquake Administration. Arrows indicate plate motion relative to stable Eurasia. Black thick and gray lines show respectively the main block-bounding faults and secondary active faults from *Deng et al.* [2003]. Yellow shading outlines the Bayan Har Block. Earthquakes since 1997 are labelled in red. Blue box outlines the area shown in b). **b)** Line-of-sight (LOS) ground displacement measured from SAR amplitude cross-correlation. Negative values indicate motion toward the satellite. Blue vectors show horizontal co-seismic displacement and 1-sigma uncertainties at the GNSS stations (black triangles). Beachball shows focal mechanism from the global centroid moment tensor solution and blue star locates the epicenter. **c)** Relocated aftershocks [*Wang et al.*, 2021] color-coded with depth, and surface projection of the faults adopted in this study (purple line).
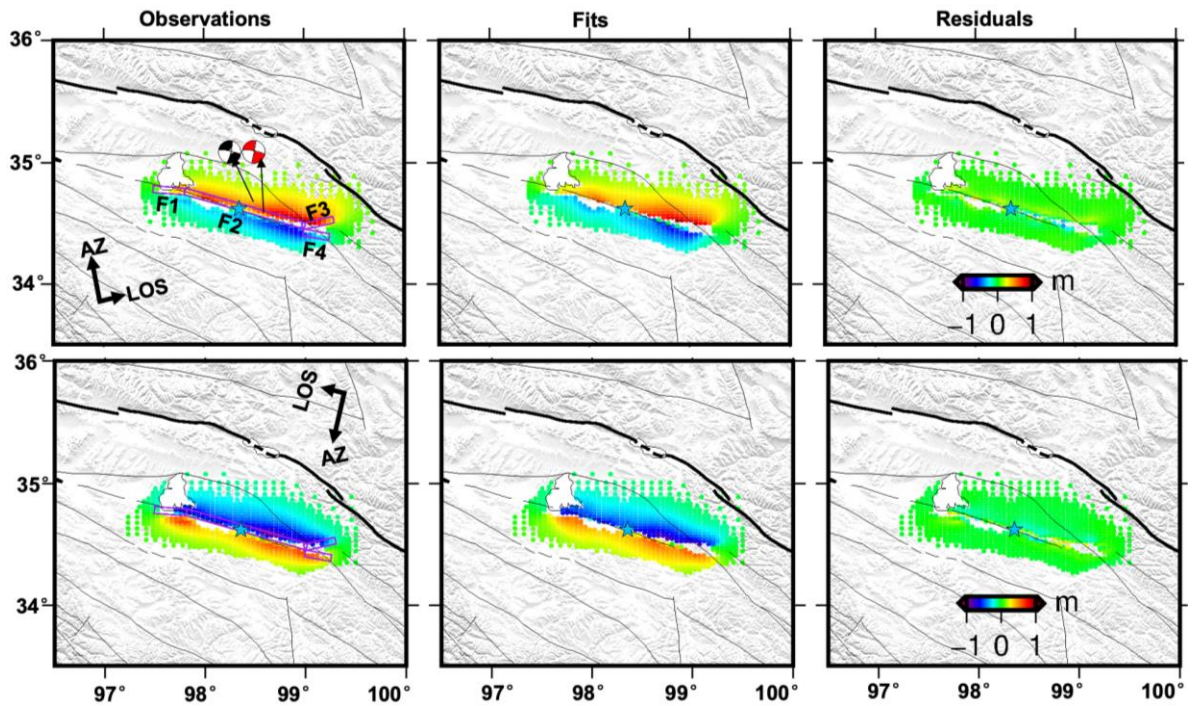
Figure 2. Sampled InSAR observations, best-fitting model and residuals for ascending (top panels) and descending track (bottom panels). Purple rectangle is the surface projection of the fault plane, blue star denotes epicenter adopted in this study. Black and red beachballs represent centroid moment tensor solutions from GCMT and this study, respectively. Black thick and gray lines are main and secondary active faults and white polygons outline the Qingling lake.
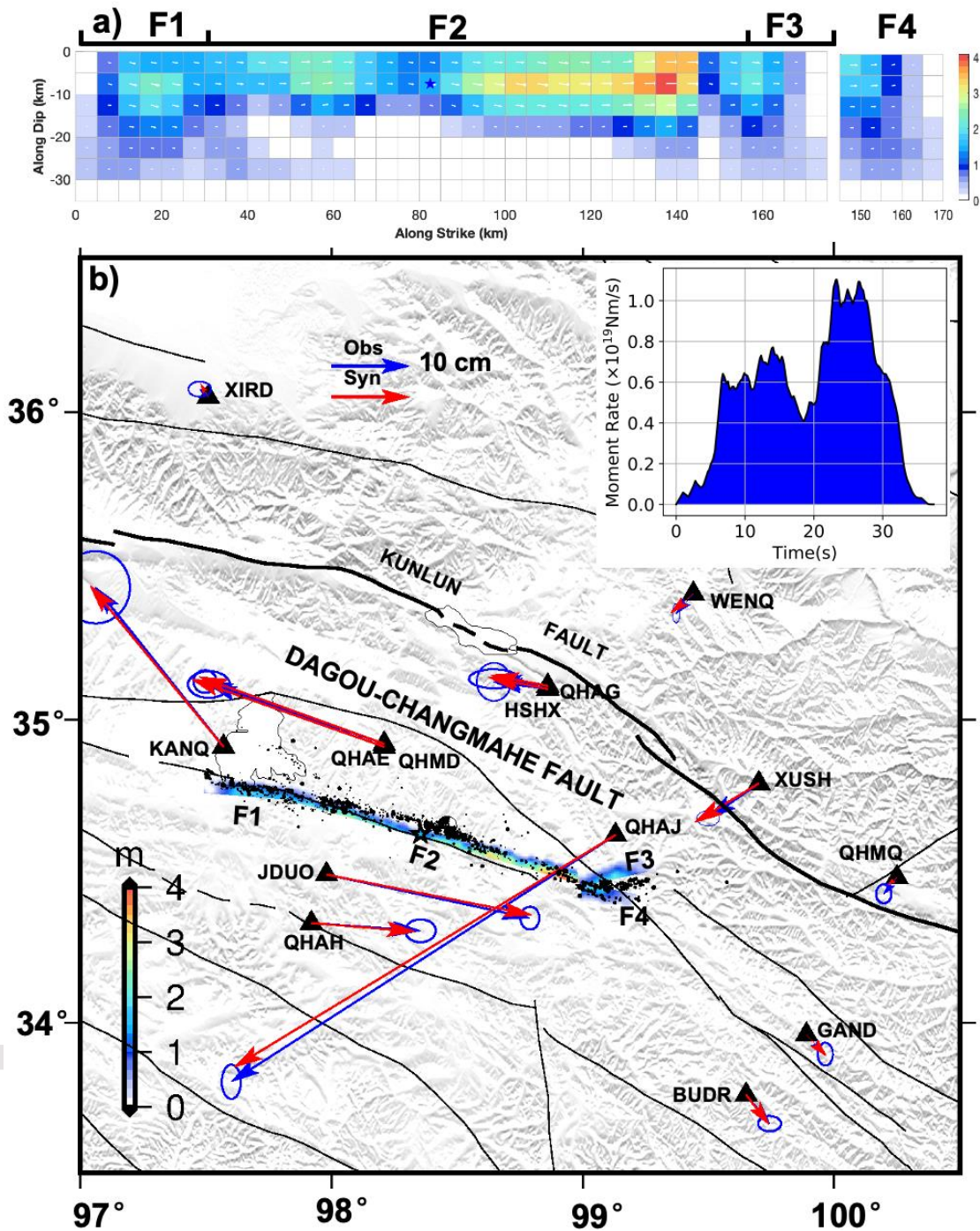
Figure 3. a) Tile view of the final slip model. Blue star locates the epicenter and the arrows show the rake angle at each patch. **b)** Comparison of measured (blue) and predicted (red) horizontal co-seismic displacements. Black dots show aftershocks determined by *Wang et al.* [2021]. Color shading shows the best-fitting co-seismic slip distribution of the 2021 Mw 7.4 Madoi earthquake from the joint inversion of all the data assembled in this study. Inset shows moment rate as a function of time.
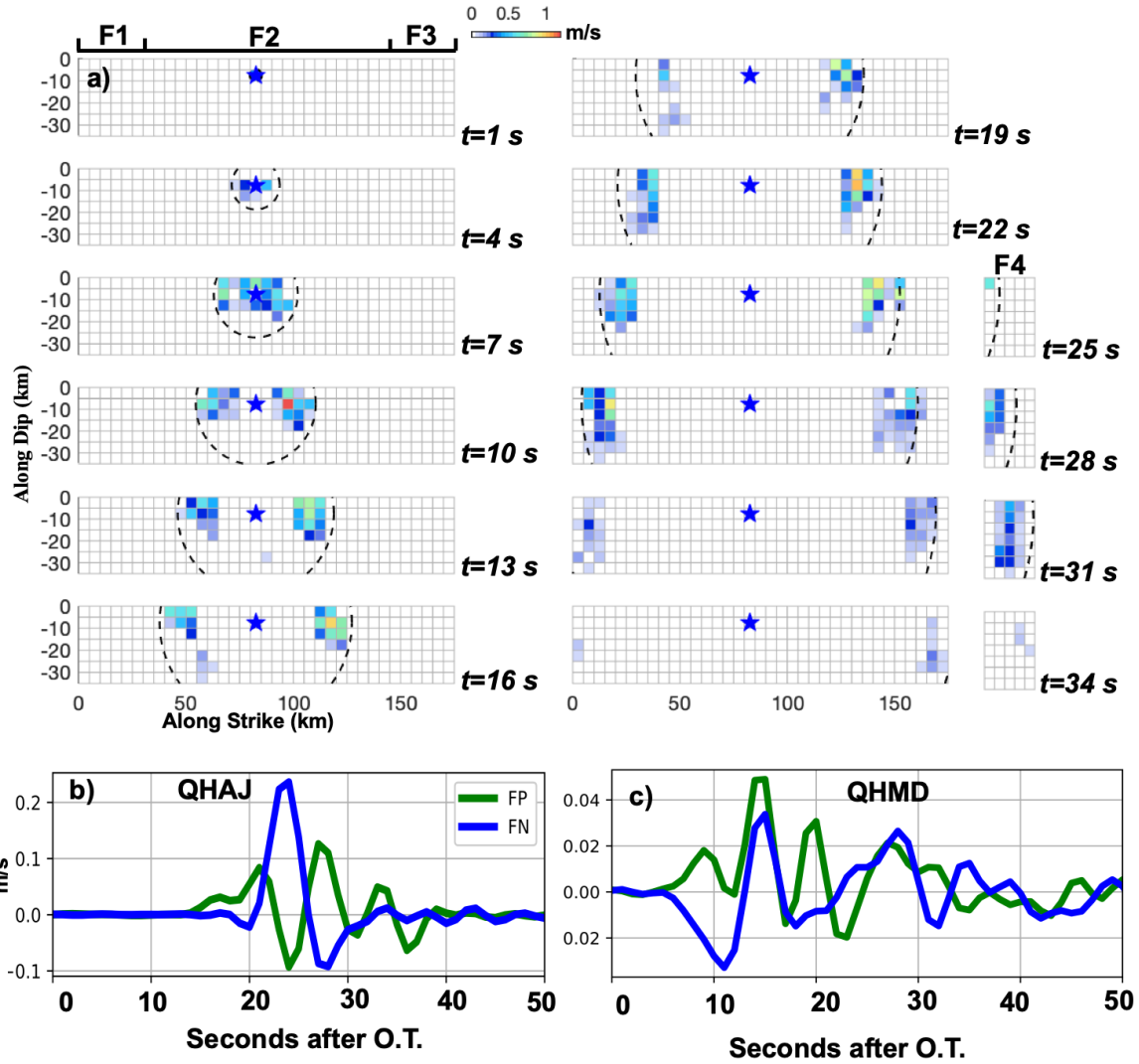
Figure 4. a) Snapshots of the rupture evolution at 3 second time intervals. Black dashed line shows the isochron of rupture front for a rupture speed of 2.8 km/s. **b)** Fault-parallel (FP) and -normal (FN) velocity at GNSS stations QHAJ and QHMD.